Geophysical Journal International

Geophys. J. Int. (2010) **183,** 1104–1118 doi: 10.1111/j.1365-246X.2010.04812.x

Spatiotemporal characteristics of aftershock sequences in the South Iceland Seismic Zone: interpretation in terms of pore pressure diffusion and poroelasticity

Mattias Lindman,* Björn Lund[1] and Roland Roberts[1]

[1] *Department of Earth Sciences, Uppsala University, Sweden*

Accepted 2010 September 16. Received 2010 September 01; in original form 2009 June 17

SUMMARY

In seismology numerous observations indicate a relationship between pore pressure in the Earth's crust and the occurrence of earthquakes. In this paper we study aftershock sequences in the South Iceland Seismic Zone (SISZ), where poroelastic rebound has been observed in the post-seismic period of two M 6.5 earthquakes in 2000 June. We analyse characteristic features in the spatiotemporal distribution of aftershocks following the two M 6.5 2000 June 17 and 21 earthquakes and a M 4.5 earthquake on 1999 September 27. These features include an initial pre-power-law decay period characterized by an initially finite aftershock rate, a subsequent power-law decay interrupted by distinct and temporary rate increases and decreases as well as increased clustering of aftershocks with time in the main shock fault zones. Extending the analysis to a M 3.2 aftershock sequence in the same region confirms an increase in the duration of the initial pre-power-law decay period with increasing main shock magnitude. We find, from the return time of aftershock magnitudes to the long-term completeness level, that the initial pre-power-law decay period and its durational dependence on main shock magnitude may not only represent incompleteness artefacts but may also reflect the physics of the aftershock process in the SISZ. Based on pore pressure diffusion modelling, we interpret the origin of the observed SISZ aftershock features in terms of a spatially non-linear coseismic influence of the main shock on stresses in the surrounding crust and poroelastic adjustment of stresses and pore pressures during main shock initiated diffusion processes. In a discussion of alternative interpretations, we find that rate and state friction and dynamically propagating crack models, the statistical ETAS model, afterslip models, viscoelastic relaxation of the lower crust and upper mantle and a recently proposed dependence on the crustal state of stress all appear inconsistent with at least one of the characteristic spatiotemporal features of the studied SISZ aftershock sequences. We conclude that these features constitute strong evidence for pore pressure effects in aftershock triggering within the SISZ and recommend that poroelastic adjustment of stresses is taken into account in modelling of main shock initiated pore pressure diffusion.

Key words: Time series analysis; Spatial analysis; Seismic cycle; Geomechanics; Seismicity and tectonics; Mechanics, theory and modelling.

1 INTRODUCTION

The Earth's crust is, at many locations, saturated with fluids that fill pores, cavities, cracks and faults and exert a pressure on the surrounding rock. In seismology numerous observations indicate a relationship between pore pressure in the crust and the occurrence of earthquakes. Circumstances where pore pressure-induced seismicity has been observed include reservoir loading (e.g. Beck 1976; Bell & Nur 1978; Talwani & Acree 1985; Roeloffs 1988; Pandee & Chadha 2003), groundwater recharge (e.g. Saar & Manga 2003), fluid injection (e.g. Zoback & Harjes 1997; Shapiro *et al.* 2003), fluid extraction (e.g. Segall 1985, 1989) and following the occurrence of large earthquakes (e.g. Nur & Booker 1972; Li *et al.* 1987; Bosl & Nur 2002; Shapiro *et al.* 2003; Gavrilenko 2005).

Nur & Booker (1972) suggest that aftershocks occur as a result of diffusion of the pore pressure transient induced by a main shock and show that a pore pressure diffusion model can explain the power-law decay in Omori's law for aftershocks (Omori 1894). Alternative hypotheses for the occurrence of aftershocks include dynamically propagating cracks (e.g. Yamashita & Knopoff 1987; Shaw 1993; Kanamori & Brodsky 2004), rate- and state-dependent frictional slip on faults (e.g. Dieterich 1994; Kanamori & Brodsky 2004), the ETAS model of secondary triggering (Ogata 1988), viscoelastic

*E-mail: mattiaslindman@yahoo.se

relaxation (e.g. Deng *et al.* 1999; Freed & Lin 2001) and afterslip (e.g. Perfettini & Avouac 2004; Hsu *et al.* 2006). The empirically well-established Omori law (Utsu *et al.* 1995) describes the temporal decay in the rate of aftershocks as (Utsu 1961).

$$\frac{\mathrm{d}n}{\mathrm{d}t} = \frac{K}{(c+t)^p}, \tag{1}$$

where n is the number of events following the main shock, K, c and p are empirical constants, and t is the time since the main shock. For a non-zero value of c, the Omori law predicts a transition from a period ($t < c$) with a constant and finite aftershock rate initially at $t = 0$ (given by K/c^p) to a period ($t > c$) with a power-law decay in the rate of aftershocks. In the subsequent discussion we refer to the initial period $t < c$ as the pre-power-law decay period. If the value of c is zero, however, the Omori law is a pure power law for all times $t > 0$, with an infinitely large initial aftershock rate at $t = 0$. By modelling pore fluid diffusion following the Landers 1992 earthquake, Bosl & Nur (2002) infer a rate of pore pressure-induced seismicity in agreement with the Omori law and the rate of the observed Landers aftershocks. The modelling of Bosl & Nur (2002) thus show that main shock initiated pore pressure diffusion is a process resulting in a rate of aftershocks that decays as a power law after an initial period governed by a finite aftershock rate, as in eq. (1) with a non-zero value of c.

Following two M 6.5 earthquakes in the South Iceland Seismic Zone (SISZ), 2000 June 17 and 21, significant water level changes took place in geothermal wells (Björnsson *et al.* 2001) and crustal deformation measured by InSAR indicated poroelastic rebound (Jónsson *et al.* 2003). These observations demonstrate that diffusion of main shock induced pore pressure transients played a significant role in geophysical and hydrological processes in the post-seismic period of these two earthquakes. Considering the role pore pressure can play in triggering earthquakes, the SISZ thus forms a natural laboratory for investigating the possible relationship between main shock initiated diffusion processes and the occurrence of aftershocks.

In this paper, we identify and analyse characteristic features in the spatiotemporal distribution of aftershocks in the SISZ, following the two M 6.5 2000 June 17 and 21 earthquakes and a M 4.5 earthquake on 1999 September 27. We also briefly discuss a M 3.2 aftershock sequence from the same region taking place on 1995 February 28. Our aim is to suggest an interpretation of the features in the studied SISZ aftershock sequences in terms of the physics of pore pressure diffusion. We model pore pressure diffusion processes initiated by main shocks of two different magnitudes, $M_\mathrm{w} = 2.2$ and $M_\mathrm{w} = 4.6$, to investigate the dependency of pore pressure-induced seismicity on main shock magnitude. In the $M_\mathrm{w} = 4.6$ case, we also consider poroelastic adjustment of both stresses and pore pressures during the diffusion process.

2 THEORY OF MAIN SHOCK INITIATED PORE PRESSURE DIFFUSION AND PORE PRESSURE TRIGGERING

Main shock initiated pore pressure diffusion processes are driven by coseismic stress and pore pressure changes in the crust surrounding the main shock. Here we describe the calculation of these stress and pore pressure changes, equations governing the associated pore pressure diffusion process, a pore pressure failure criterion derived from the Mohr–Coulomb failure criterion and pore pressure triggering of seismicity during the diffusion process.

2.1 Coseismic stress and pore pressure changes

Following Rice & Cleary (1976), the coupled constitutive equations that relate strain, stress, pore pressure and fluid mass content per unit volume for an isotropic fluid saturated medium are

$$2G\varepsilon_{ij} = \sigma_{ij} - \frac{\nu}{1+\nu_u}\sigma_{kk}\delta_{ij} - \frac{3(\nu_u-\nu)}{B(1+\nu)(1+\nu_u)}P\delta_{ij}, \tag{2}$$

$$m - m_0 = \frac{3\rho_0(\nu_u-\nu)}{2GB(1+\nu)(1+\nu_u)}\left[\sigma_{kk} - \frac{3}{B}P\right], \tag{3}$$

where the Einstein summation convention applies and ε_{ij} are strains, σ_{ij} stresses, P pore pressure, $m - m_0$ change in fluid mass content per unit volume, ρ_0 fluid density, G shear modulus, ν and ν_u drained and undrained Poisson's ratio and B Skempton's coefficient. The indices i and j runs over the coordinate directions E, N and Z.

The static elastic strain and stress changes during an earthquake are assumed to take place so rapidly that there is no net fluid flow. The induced coseismic pore pressure change is therefore given by setting $m - m_0 = 0$ in eq. (3), yielding $\Delta\sigma_{kk} = (3/B)\cdot\Delta P_\mathrm{ind}$. Inserting this into eq. (2) and rewriting, the coseismic change in pore pressure can be written in terms of the volumetric strain change caused by the earthquake:

$$\Delta P_\mathrm{ind} = \frac{B}{3}\frac{2G(1+\nu_u)}{1-2\nu_u}\Delta\varepsilon_{kk}. \tag{4}$$

We can also use $\Delta P_\mathrm{ind} = (B/3)\,\sigma_{kk}$ to rewrite eq. (2) to give the coseismic stress change in terms of the elastic deformation due to an earthquake:

$$\Delta\sigma_{ij}^\mathrm{ind} = 2G\left(\Delta\varepsilon_{ij} + \frac{\nu_u}{1-2\nu_u}\Delta\varepsilon_{kk}\delta_{ij}\right). \tag{5}$$

In our calculations, we assume a volume decrease to be positive and induced compressional stresses will thus be positive. Note though, that Rice & Cleary (1976) treat compressional stresses as negative and dilatational stresses as positive. To calculate coseismic changes in pore pressures (eq. 4) and stresses (eq. 5) we use the equations of Okada (1992) to calculate elastic deformations associated with a main shock slip model.

2.2 Diffusion equations

2.2.1 Pore pressure diffusion equation

In hydrogeological applications it is often assumed that the strain is purely vertical and that the Earth's surface is a free surface with no changes in the overburden pressure. Assuming an isodense and isoviscous fluid, no significant elevation changes over time and incompressible solid grains, the diffusion of coseismically induced pore pressure changes is governed by the equation

$$D\nabla^2(\Delta P_\mathrm{ind}) = \frac{\partial}{\partial t}(\Delta P_\mathrm{ind}), \tag{6}$$

where ΔP_ind is the induced pore pressure transient (eq. 4) and the hydraulic diffusivity D is given by

$$D = \frac{k}{\eta\left(\frac{1+\nu}{3(1-\nu)K} + \phi\frac{1}{K_f}\right)}, \tag{7}$$

where k is the permeability, η the dynamic viscosity of the fluid, ϕ the porosity and K_f the fluid bulk modulus (Neuzil 2003).

2.2.2 Poroelastic diffusion equation

Using Darcy's law for the isotropic case, strain and stress compatibility equations, force equilibrium and conservation of fluid mass, Rice & Cleary (1976) obtain a diffusion equation of the form

$$c_m \nabla^2 \left(\Delta\sigma_{kk} - \frac{3}{B}\Delta P \right) = \frac{\partial}{\partial t}\left(\Delta\sigma_{kk} - \frac{3}{B}\Delta P \right), \tag{8}$$

where c_m is the hydraulic diffusivity given by

$$c_m = \frac{1}{3}\frac{k}{\eta}\left[\frac{2G(1-\nu)}{(1-2\nu)}\right]\left[\frac{B^2(1+\nu_u)^2(1-2\nu)}{9(\nu_u-1)(\nu_u-\nu)}\right], \tag{9}$$

where k is permeability and η is the dynamic viscosity of the fluid.

The poroelastic diffusion equation (eq. 8) implies poroelastic adjustment of stresses as coseismic pore pressure changes return to equilibrium during the diffusion process.

In eq. (8), $\Delta\sigma_{kk}$ refers to a stress perturbation ($\Delta\sigma_{ij}$) satisfying force equilibrium and strain and stress compatibility equations. This stress perturbation can be determined by solving the following set of equations (for a treatment of their derivation, see e.g. Wang 2000; Neuzil 2003):

$$\nabla^2 \left(\Delta\sigma_{kk} - \frac{6(\nu_u-\nu)}{B(1-\nu)(1+\nu_u)}\Delta P \right) = 0 \tag{10}$$

$$\nabla^2 \left((1+\nu)\Delta\sigma_{ij} - \nu\Delta\sigma_{kk}\delta_{ij} \right) + \frac{\partial^2 \Delta\sigma_{kk}}{\partial x_i \partial x_j} - \\ - \frac{3(\nu_u-\nu)}{B(1+\nu_u)}\left(\frac{\partial^2 \Delta P}{\partial x_i \partial x_j} + \nabla^2(\Delta P)\delta_{ij} \right) = 0 \tag{11}$$

2.3 Pore pressure failure criterion

To evaluate the seismicity induced by a main shock initiated pore pressure diffusion process we utilize the Mohr–Coulomb failure criterion (e.g. Scholz 2002)

$$\tau_f = \tau_0 + \mu(\sigma_n - P), \tag{12}$$

where τ_f is the shear stress required to overcome the shear strength of a fault, τ_0 a cohesion term, μ the coefficient of friction, σ_n the normal stress on the fault and P the pore pressure. Note that σ_n and P here refer to total stresses and pore pressures. The Mohr–Coulomb failure criterion can be rewritten in terms of a pore pressure failure criterion which we use to evaluate pore pressure-induced seismicity. Assuming the cohesion τ_0 to be zero (see e.g. Brace & Kohlstedt 1980; Zoback & Healy 1984) and that failure will take place on faults optimally oriented for failure in relation to the total stress state, the critical pore pressure necessary for failure is

$$P_{\text{crit}} = \frac{1}{2\mu}\left[-\sigma_1\left((1+\mu^2)^{1/2} - \mu \right) + \sigma_3\left((1+\mu^2)^{1/2} + \mu \right) \right], \tag{13}$$

where σ_1 and σ_3 are the principal stresses of the total stress state having the largest and smallest magnitudes, respectively.

2.4 Pore pressure triggering during the diffusion process

In our modelling the total stress state is the sum of a background state of stress and a stress perturbation, where the stress perturbation can be the coseismic stress change (eq. 5) or the time-dependent poroelastic stress perturbation (eqs 10 and 11). To obtain a non-zero pore pressure triggering rate in our modelled diffusion processes an essential requirement is that at least some part of the crust is in a critical state initially, with optimally oriented faults on the point of failure according to the Mohr-Coulomb failure criterion (eq. 12). We assume that the background state of stress, prior to any stress and pore pressure perturbation, is critical in the entire crust (see Section 4.1.2). This implies that the background stress state yields a critical pore pressure that is equivalent to the undisturbed regional pore pressure P_{reg}.

Now, a perturbation of the background stress state implies that the critical pore pressure necessary for failure will also be perturbed. If we assume post-seismic pore pressure diffusion only (eq. 6), the coseismically perturbed critical pore pressure ($P_{\text{crit}}^{\text{pert}}$) does not change with time during the diffusion process. Given $P_{\text{crit}}^{\text{pert}}$, the regional pore pressure P_{reg} and the coseismic pore pressure perturbation ΔP_{ind} the diffusion process will trigger seismicity in the parts of the crust where

$$P_{\text{reg}} + \Delta P_{\text{ind}} < P_{\text{crit}}^{\text{pert}} < P_{\text{reg}}. \tag{14}$$

From eq. (14) we can see that triggering will take place in the dilatational regime of the main shock as the coseismic pore pressure perturbation has to reduce the regional pore pressure for the above relationship to hold. We can thus use eq. (14) to determine the spatial extent of potential triggering and the dimensions of the volume where we need to model the pore pressure diffusion process. During the diffusion process pore pressures will recover by rising in the dilatational regime and trigger seismicity when the sum of the diffusing pore pressure transient and the regional pore pressure exceeds the critical pore pressure.

3 ANALYSIS OF AFTERSHOCK SEQUENCES IN THE SISZ

In Iceland, the onland spreading of the mid-Atlantic Ridge is offset by two east–west oriented transform zones, the SISZ in the south and the Tjörnes Fracture Zone off the north coast. The SISZ stretches 70–80 km eastwards from the Hengill triple junction and accommodates left-lateral transform motion between the North American and the Eurasian plates. This motion, however, is not accommodated by a major E–W oriented strike-slip fault. Instead, the SISZ accommodates the plate motion through right-lateral strike-slip faulting on vertical north–south striking faults. It has been suggested that bookshelf tectonics is responsible for this way of accommodating the plate motion, with counter-clockwise rotation of blocks between N–S oriented right-lateral strike-slip faults (Einarsson 1991).

3.1 Data

3.1.1 Spatial distribution of main shocks and aftershocks

Fig. 1 shows the locations and focal mechanisms of the main shocks whose aftershock sequences we study in this paper. The Harvard CMT focal mechanisms of the 2000 June 17 (J17) and 21 (J21) M 6.5 earthquakes are of the type expected for the SISZ, with right-lateral strike-slip faulting on north–south striking faults. For the M 4.5 event on 1999 September 27 (S27) and the M 3.2 event on 1995 February 28 (F28) the corresponding focal mechanisms indicate (according to the Icelandic Meteorological Office database) oblique normal slip on roughly east–west oriented faults or left-lateral oblique slip on roughly north–south oriented faults.

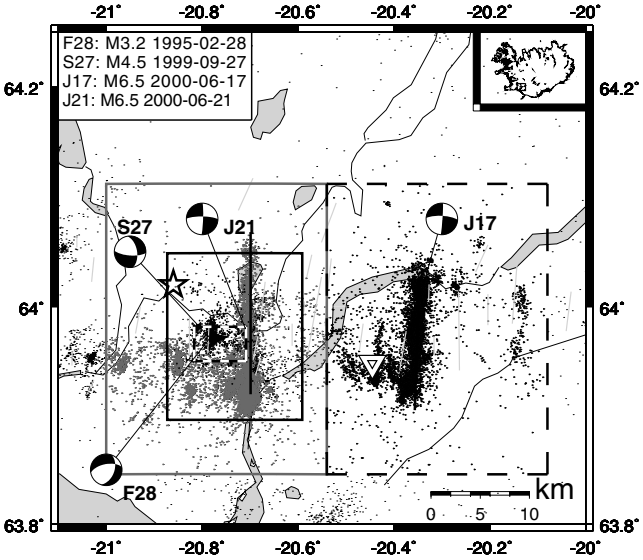

Figure 1. Investigated main shocks in the South Iceland Seismic Zone (SISZ), their focal mechanisms, and spatial distribution of corresponding aftershocks. Seismicity within the inner solid black frame (black dots): *M* 4.5 1999 September 27 (S27) aftershocks, within the dashed black frame (black dots): *M* 6.5 2000 June 17 (J17) aftershocks, within the grey frame (grey dots): *M* 6.5 2000 June 21 (J21) aftershocks. The dashed black and white frame (inside the inner solid black frame) delimits the spatial extent of aftershocks associated with a *M* 3.2 main shock on 1995 February 28 (F28). Star: a $M \sim 3.5$ earthquake occurring within the first 30 s of the J17 earthquake. Inverted triangle: a $M \sim 5$ earthquake occurring 2 min after the J17 earthquake. Inset: the location of the SISZ.

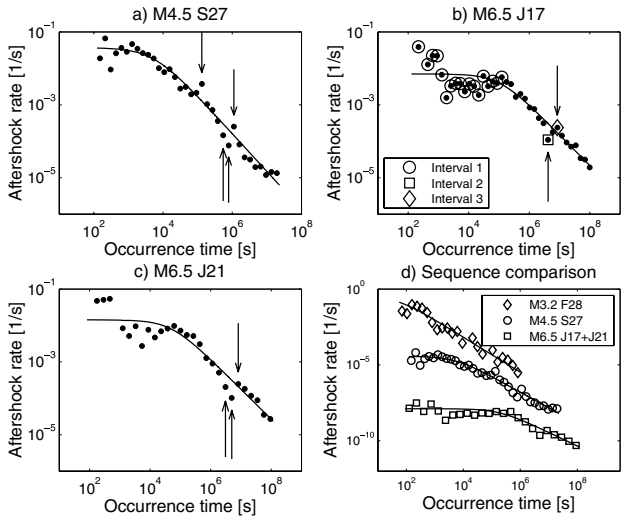

Figure 2. (a), (b) and (c): rate of aftershocks versus time (black dots) for (a) the *M* 4.5 S27 aftershock sequence, (b) the *M* 6.5 J17 aftershock sequence and (c) the *M* 6.5 J21 aftershock sequence. Upward- and downward-pointing arrows: bins exhibiting significant deviations from the Omori power-law decay in terms of drops and increases in aftershock rate (see Section 3.1.2). In (b) the bins marked by circles, a square and a diamond indicate time intervals (the first *c* seconds, day 46–50 and day 91–95, respectively) during which Fig. 4 shows spatial snapshots of the *M* 6.5 J17 aftershocks. (d): seismicity rate versus time for the *M* 3.2 F28 (diamonds), the *M* 4.5 S27 (circles) and the combined *M* 6.5 J17+J21 (squares) aftershock sequences. The rate curves are shifted on the vertical axis for clarity. In (a)–(d) the solid black curves represent the Omori law using the values of K, c and p estimated from each sequence.

The spatial extent of the studied aftershock sequences is defined by the different frames shown in Fig. 1. Within these frames our defined aftershock sequences consists of detected earthquakes in time periods starting immediately after respective main shock and ranging up to ∼11 d (*M* 3.2 F28), ∼8.5 months (*M* 4.5 S27) and ∼3.7 yr (*M* 6.5 J17 and *M* 6.5 J21). The seismicity (plotted in black) within the inner black frame surround the *M* 4.5 S27 epicentre and represent earthquakes defined as *M*4.5 S27 aftershocks. Within the dashed black and grey frames the plotted seismicity represents earthquakes defined as *M* 6.5 J17 (black dots) and *M* 6.5 J21 (grey dots) aftershocks. Finally, the black and white dashed frame shows the spatial extent of aftershocks associated with the *M* 3.2 F28 main shock. In the subsequent discussion we refer to the defined sequences as the *M* 3.2 F28, *M* 4.5 S27, *M* 6.5 J17 and *M* 6.5 J21 aftershock sequences, respectively.

The *M* 6.5 J17 and *M* 5.6 J21 aftershock sequences are considered as separate sequences in our spatiotemporal analysis of the corresponding aftershock distributions. We may, however, also consider the *M* 6.5 J21 main shock and its aftershocks in the J21 frame as aftershocks of the *M* 6.5 J17 main shock. We have thus also defined a combined aftershock sequence, including events from both the J17 and J21 frames in a ∼3.7-year period following the *M* 6.5 J17 main shock. Later, we refer to this combined sequence as the *M* 6.5 J17+J21 sequence.

In Fig. 1, the star shows the location of a $M \sim 3.5$ earthquake occurring within the first 30 s of the *M* 6.5 J17 earthquake (Antonioli *et al.* 2006). By modelling the dynamic stress perturbations associated with the passing of the seismic waves of the J17 earthquake and using a fault response governed by rate and state-dependent friction, Antonioli *et al.* (2006) conclude that the occurrence of this event may be explained by instantaneous dynamic triggering. Following this event an earthquake with $M \sim 5$, shown by the inverted triangle in Fig. 1, took place 2 min after the *M* 6.5 J17 earthquake, just west of the J17 fault (Vogfjord 2003). This aftershock will be discussed shortly in Section 3.2.

3.1.2 Aftershock rate

The decay in the rate of aftershocks with time in the *M* 4.5 S27, *M* 6.5 J17 and *M* 6.5 J21 aftershock sequences is shown in Figs 2(a)–(c), respectively. These plots show, in general, that the aftershock rate in all of the sequences obeys the Omori law, with an initial pre-power-law decay period during approximately *c* seconds and a subsequent power-law decay. During the pre-power-law decay period there are quite large fluctuations in aftershock rate around the rate predicted by the Omori law. This may be a result of random sampling biases due to potential masking shortly after respective main shock (see Section 3.1.3).

Considering the combined *M* 6.5 J17+J21 sequence Fig. 2(d) shows that the seismicity rate following the *M* 6.5 J17 main shock within the combined J17 and J21 frames also obeys the Omori law. For comparison, Fig. 2(d) also shows the seismicity rate in the *M* 3.2 and *M* 4.5 S27 aftershock sequences. Comparing the sequences in Fig. 2(d) with each other we can see that the duration of the pre-power-law decay period increases with increasing main shock magnitude. This dependency on main shock magnitude is also indicated in Figs 2(a)–(c), as the duration of the pre-power-law decay period is much shorter in the *M* 4.5 S27 aftershock sequence than in the two *M* 6.5 J17 and *M* 6.5 J21 aftershock sequences.

By carefully studying the power-law decay period, we can identify a common feature among the aftershock sequences, marked by the

upward-pointing arrows in Figs 2(a)–(c). This feature is a distinct drop in the rate of aftershocks, below the expectation value of the rate given by the Omori law for each sequence. For the *M* 4.5 S27, *M* 6.5 J17 and *M* 6.5 J21 sequences, this lower rate of aftershocks can be seen in histogram bins covering the time between 5.2–10.5, 40–57 and 27–72 days after each main shock, respectively. Here, day refers to the number of 24-hr periods counted from the occurrence time of respective main shock. We will use this definition of day throughout the remainder of this paper.

Following these drops, the rate increases significantly (marked by downward-pointing arrows in Figs 2a–c) and the power-law decay is then resumed, closely following the Omori law for the rest of each sequence. For the *M* 4.5 S27, *M* 6.5 J17 and *M* 6.5 J21 sequences, these rate increases can be seen in histogram bins covering the time between 10.5–15.2, 57–115 and 72–117 days after each main shock, respectively. A rate increase that is not preceded by a distinct drop in the seismicity rate can also be seen early in *M* 4.5 S27 sequence, in a histogram bin covering the time between 1.25–1.8 days after the main shock.

To interpret the origin of the distinct rate drops (and subsequent rate increases) we need to assess whether the drops in aftershock rate are statistically significant. We use a Monte Carlo approach to assess whether we can reject the hypothesis that the distinct rate drops is a result of random fluctuations in respective aftershock sequence. First we assume that the rate of aftershocks is governed by the Omori law (with maximum likelihood estimates of the parameters K, c and p). Monte Carlo simulations of each aftershock sequence using the stretching algorithm (Jónsdottir *et al.* 2006) then reveals that we, with a confidence level over 99.99 per cent, can reject the hypothesis that the distinct rate drops are caused by random fluctuations in aftershock processes governed by the Omori law.

We may interpret the distinct rate drops and subsequent rate increases in terms of the statistical ETAS model of seismicity (Ogata 1988), in which each aftershock has a magnitude-dependent ability to trigger its own aftershocks with a rate decaying according to the Omori law. Monte Carlo simulations using an ETAS model shows that we cannot reject the hypothesis that the distinct rate drops and subsequent rate increases are due to secondary triggering. We can only reject the ETAS hypothesis by showing that there is no nearby large aftershock during the nearest time period prior to a distinct rate increase. For each of the *M* 4.5 S27, *M* 6.5 J17 and *M* 6.5 J21 aftershock sequences we have thus made a careful analysis of how aftershock magnitudes and number of aftershocks varies with time in crustal volumes where aftershocks cluster during the rate increases that follow the distinct rate drops. This analysis is illustrated in Section 3.2 for the *M* 6.5 J17 aftershock sequence and the result is summarized in Section 3.3, point (viii).

3.1.3 Temporal completeness

After a larger earthquake the seismic activity will be intense in the fault zone and the near fault zone region. As this may lead to masking of small aftershocks in the coda associated with the main shock (and possibly also larger aftershocks) it is inevitable that our observations of the beginning of aftershock sequences will be incomplete to some extent. It has been shown, for aftershock sequences in Japan (Nanjo *et al.* 2007) and California (Shcherbakov *et al.* 2004), that reducing the cut-off magnitude to include smaller aftershocks prolongs the onset of the power-law decay in aftershock rate. The initial pre-power-law decay period (and the associated non-zero value of the Omori law parameter c) is therefore often considered an artefact of incomplete detection of small aftershocks (e.g. Utsu *et al.* 1995; Kisslinger 1996; Kagan 2004; Woessner *et al.* 2004; Kagan & Houston 2005; Lolli & Gasperini 2006). It has been observed, however, that non-zero c-values obtained when restricting the analysis to smaller main shock- and larger aftershock magnitudes reflect a systematic behaviour of early aftershocks rather than incompleteness artefacts (Narteau *et al.* 2009).

That it is necessary to assess the duration of the masking period is demonstrated by the recovery of a significant number of small, mostly undetected, aftershocks from high-pass filtered seismograms covering limited time periods immediately following main shocks in Japan (e.g. Enescu *et al.* 2007; Peng *et al.* 2007) and the 2004 *M*w 6.0 Parkfield, California, earthquake (Peng *et al.* 2006). With main shocks of different magnitudes (as in this study) it is natural to expect that the duration of the masking period increases with increasing main shock magnitude (e.g. Lennartz *et al.* 2008). To assess this duration using high-pass filtered waveform data it is necessary to determine when the ratio between the cumulative number of aftershocks recorded in the network catalogue and detected in the high-pass filtered waveforms reaches the value of 1. If this ratio reaches the value of 1 before $t = c$ it implies that the non-zero value of c is not an incompleteness artefact and may reflect the physics of the aftershock process.

In this study we take another approach, utilizing recorded aftershock magnitudes, to assess the duration of the potential masking period as the required waveform data to perform the above analysis is unavailable to us. For a given earthquake data set, the magnitude of completeness (M_c) is typically defined as the magnitude above which the magnitude distribution is well described by the empirical Gutenberg-Richter law (Gutenberg & Richter 1944). We assess long-term M_c levels prior to each of the main shocks in this study, using earthquakes in the time periods 1992 January 1 to 1999 September 27 (within the *M* 4.5 S27, *M* 6.5 J17, *M* 6.5 J21 and *M* 6.5 J17+J21 frames in Fig. 1) and 1992 January 1 to 1995 February 28 (within the *M* 3.2 F28 frame in Fig. 1). To estimate M_c levels for the corresponding aftershock sequences we use magnitudes of detected aftershocks in the time interval of each sequence (see Section 3.1.1). The result is listed in Table 1 where we can see that the estimated M_c level for the studied aftershock sequences is always larger than the corresponding long-term M_c level. This implies that we cannot use the point in time when aftershocks are complete down to the long-term completeness magnitude M_c to estimate the masking period (as the recorded aftershock sequences does not provide this information). Instead, we consider the return time of aftershock magnitudes to the long-term M_c level as an estimate of the duration of the masking period for each aftershock sequence.

In Figs 3(a), (b) and (d) we can see that the minimum magnitude in equal-sized temporal bins returns to the long-term completeness level at times $t < c$ in the *M* 4.5 S27, the *M* 6.5 J17 and the combined *M* 6.5 J17+J21 aftershock sequences. For both the *M* 4.5 S27 and the combined *M* 6.5 J17+J21 aftershock sequences in Figs 3(a) and (d) the minimum magnitude then drops below the long-term completeness level before $t = c$. In the *M* 6.5 J17 sequence, however, the minimum magnitude drops below this level first after $t = c$. Finally, the return time is approximately equal to the value of c in the *M* 6.5 J21 aftershock sequence, as shown in Fig. 3(c). For the *M* 3.2 F28 aftershock sequence we do not perform this analysis as the first recorded aftershock occurs at a time t that is greater than the associated c value. In this sequence, however, masking of small aftershocks is unlikely due to the low main shock magnitude.

Table 1. Omori law c values (maximum likelihood estimates) and magnitude of completeness levels for the studied aftershock sequences. Except where indicated M_c is a maximum likelihood estimate assuming a truncated normal distribution below M_c and the Gutenberg–Richter law above M_c (Woessner & Wiemer 2005). Bold c values estimated using all detected aftershocks. For the M 4.5 S27 and M 6.5 J17+J21 sequences the c values obtained when excluding the potential masking period from Fig. 3 are also shown.

Sequence	c	Aftershock M_c	Long-term M_c
M 3.2 F28	**44 s**	∼0.4[a]	0.2[b]
M 4.5 S27	**5295 s**	0.35	0.1
	(∼1.5 hr)		
	$t > 0.24\ c$:		
	5422 s		
	(∼1.5 hr)		
M 6.5 J17	**104 219 s**	0.35	0.25
	(∼1.2 d)		
M 6.5 J21	**49 306 s**	0.35	0.1
	(∼13.7 hr)		
M 6.5 J17+J21	**180 500 s**	0.35	0.2
	(∼2.1 d)		
	$t > 0.35\ c$:		
	86 211 s		
	(∼1 d)		
	$t > 0.65\ c$:		
	0 s		

[a]Not well defined, the magnitude distribution does not agree well with the Gutenberg-Richter law. [b]Estimated visually from a histogram of earthquake magnitudes.

Altogether, we find that the duration of the potential masking period of small aftershocks is ∼24 per cent of the c value for the M 4.5 S27 sequence, between ∼60–100 per cent of the c value for the M 6.5 J17 sequence, ∼110 per cent of the c value for the M 6.5 J21 sequence and ∼35–65 per cent of the c value for the combined M6.5 J17+J21 sequence. For the M6.5 J17 and J21 sequences this implies that we cannot reject the null hypothesis that a non-zero c value represents an incompleteness artefact in favour of a physical interpretation. For the M 4.5 S27 and M 6.5 J17+J21 sequences, however, we may reject incompleteness artefacts as the duration of the potential masking period is shorter than the corresponding c values. Table 1 shows that removing the aftershocks during the potential masking period of the M 4.5 S27 sequence does not have a significant effect on the c value. In the M 6.5 J17+J21 sequence, however, Table 1 shows that such a removal reduces the c value with ∼50–100 per cent. Based on these findings we conclude that the increase in c value with increasing main shock magnitude expressed by the M 3.2 F28, the M 4.5 S27 and to some extent the combined M 6.5 J17+J21 aftershock sequences may not only represent incompleteness artefacts but may also reflect the physics of the aftershock process in the SISZ.

3.2 Spatiotemporal evolution of the M 6.5 J17 aftershock sequence

We have investigated the spatiotemporal evolution of the M 4.5 S27, M 6.5 J17 and M 6.5 J21 aftershock sequences by time stepping through each sequence in a consistent manner. Before summarizing the general findings from this investigation (next section), we here use the M 6.5 J17 aftershock sequence to illustrate our analysis.

Fig. 4 shows three temporal snapshots of the spatial distribution of M 6.5 J17 aftershocks, taken during (1) the first $c = 104\,219$ s

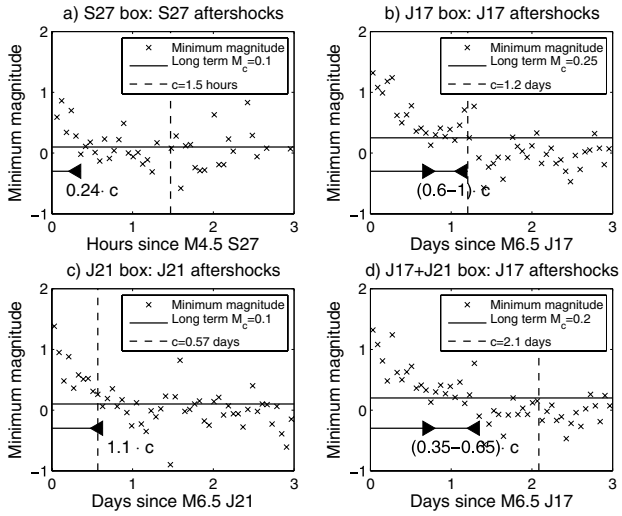

Figure 3. Minimum magnitude of aftershocks in equal-sized temporal bins for: (a) the first 3 hr of the M 4.5 S27 aftershock sequence, (b) the first 3 d of the M 6.5 J17, (c) M 6.5 J21 and (d) the combined M 6.5 J17+J21 aftershock sequences. For each aftershock sequence the horizontal lines marks the long-term magnitude of completeness (solid line) and the approximate duration of the masking period of small aftershocks (solid line with triangles). The estimated duration of the masking period is expressed in fractions of the Omori law c value for each sequence, which is shown by the vertical dashed line.

(∼29 hr) of the aftershock sequence (a and b), (2) a distinct drop in aftershock rate (day 46–50, c and d) and (3) the subsequent rate increase (day 91–95, e and f). The selected time intervals are indicated in Fig. 2(b). In Fig. 4 the left-hand panels represent a map view of the aftershocks while the right-hand panels represent aftershocks projected onto a west–east depth slice. Using the P-wave radiation pattern of the M 6.5 J17 main shock we determine the proportion of aftershocks in the dilatational and compressional quadrants for each time interval. Based on an evaluation of counting errors (see e.g. Greenhough & Main 2008) these proportions are given with two significant figures in the legend in each of the right-hand panel plots in Fig. 4.

During the first c seconds of the M 6.5 J17 aftershock sequence we can see (Figs 4a and b) some clustering close to the J17 fault (outlined by the solid frame), but also that aftershocks occur further away from the fault zone. In the depth section (Fig. 4b), it is interesting to note that the scattered aftershocks west of the fault tend to be located at depths greater than 5 km while corresponding aftershocks east of the fault tend to be located above 5 km depth. We can also see that the majority of the aftershocks occur in quadrants of coseismic dilatation and pore pressure decrease (59 per cent).

When the M 6.5 J17 aftershock rate exhibits a distinct rate drop (day 46–50), Figs 4(c) and (d) show that most of the M 6.5 J17 aftershocks are now located in the vicinity of the J17 fault plane, although some scattered seismicity exists east of the J17 fault. West of the J17 fault, Fig. 4(d) also shows some seismicity lined up along the likely fault plane of the $M \sim 5$ event taking place 2 min after the J17 earthquake. In this time interval, a clear majority (81 per cent) of the aftershocks is located in quadrants of coseismic dilatation.

During the subsequent rate increase (day 91–95), Figs 4(e) and (f) show that the M 6.5 J17 aftershocks are mainly concentrated in two clusters. Aftershocks located in the vicinity of the J17 fault form one of the clusters and aftershocks off the fault in the southwestern coseismic dilatational quadrant form the other. From Figs 4(e) and

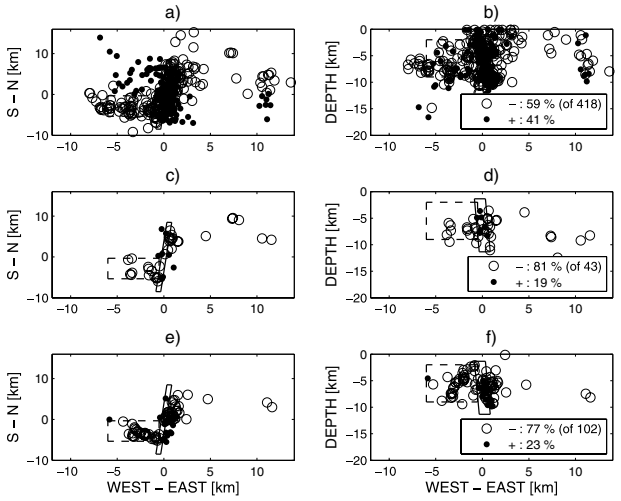

Figure 4. Spatial distribution of M 6.5 J17 aftershocks during the first $c = 104219$ s (a and b), day 46–50 (c and d) and day 91–95 (e and f). These time intervals are indicated with circles, squares and diamonds in Fig. 2(b). The horizontal aftershock coordinates (E & N) are measured relative to the M 6.5 J17 epicentre. Left panel (a, c and e): map view of M 6.5 J17 aftershocks. Right panel (b, d and f): looking from south at aftershocks projected on an west–east depth slice. Black solid frame: indicates (in both panels) the orientation of the M 6.5 J17 fault plane from the Harvard CMT focal mechanism. Black dashed frames in the left and right panels: outline a volume where aftershocks cluster during day 91–95, in part responsible for the rate increase indicated in Fig. 2(b). The legend states the number of aftershocks during each time interval and how they are distributed between main shock quadrants of coseismic dilatation (open circles, −) and compression (black dots, +).

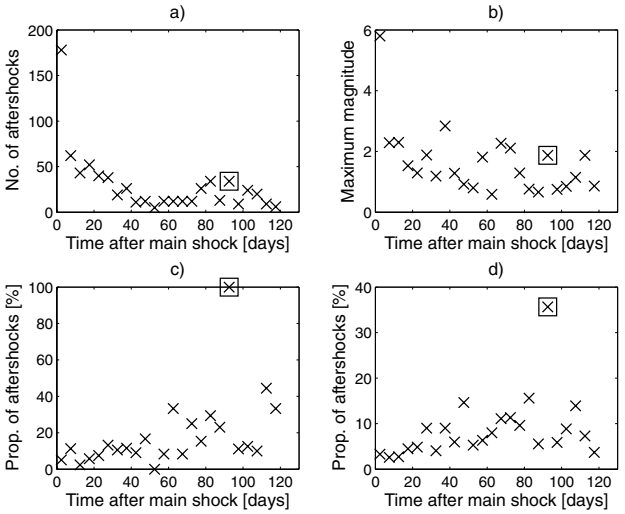

Figure 5. (a) and (b): number of aftershocks (a) and maximum magnitude (b) versus time (five-day bins) for M 6.5 J17 aftershocks within a volume spanning an aftershock cluster during day 91–95 (dashed frames in Figs 4e and f). (c) and (d): proportion of M 6.5 J17 aftershocks in the volume occupied by the aftershocks in the day 91–95 cluster versus time, considering aftershocks within the day 91–95 cluster volume (c) and within the entire M 6.5 J17 aftershock region (d). In each subplot the square indicates day 91–95.

(f) we can see that the off-fault aftershock cluster forms an elongated structure that dips to the northwest.

For each of the time intervals in Fig. 4 we assess whether the observed spatial distribution of aftershocks differ significantly from a spatially uniform distribution, with 50 per cent of the aftershocks expected in the dilatational quadrants and 50 per cent in the compressional. Given the observed number of aftershocks, we perform 10 000 random realizations of aftershocks uniformly distributed over the focal sphere of the M 6.5 J17 main shock and determine the resulting distribution of aftershock proportions in the dilatational and compressional quadrants. From this we find that the observed aftershock proportions presented in Fig. 4 all differ from a spatially uniform distribution with a confidence level well over 99 per cent, both in the dilatational and the compressional quadrants. Performing the same analysis for the entire M 6.5 J17 aftershock sequence yields a similar result.

The observed aftershock proportions in the dilatational and compressional quadrants are influenced in a random way by errors in main shock location and in a systematic way by errors in the focal mechanism. To assess the effect of focal mechanism errors we investigated how errors in main shock strike affected the observed proportions. This analysis shows that clockwise errors in strike reduces the proportion of aftershocks in the dilatational quadrants while anticlockwise errors increases this proportion. We also find that the location of the off-fault aftershock cluster in the southwestern dilatational quadrant is unaffected by clockwise errors in main shock strike up to $\sim 20^\circ$ and anticlockwise errors up to $\sim 40^\circ$. This indicates that the location of off-fault aftershocks in the dilatational quadrants (primarily the southwestern one) is a robust observation with respect to errors in the strike of the J17 main shock.

We now investigate, in more detail, the off-fault aftershock cluster during day 91–95 after the M 6.5 J17 main shock by defining a rectangular volume spanning this cluster (dashed frames in Figs 4a–f). As discussed in Section 3.1.2 the motivation for this analysis is to assess whether the ETAS model of secondary triggering may explain the increase in aftershock rate during day 91–95. Fig. 5(a) shows that the number of M 6.5 J17 aftershocks within the day 91–95 cluster volume decays in a monotonic fashion with time during the first $\sim$75 days after the mainshock. Then the number of aftershocks exhibits three peaks, during day 81–85, day 91–95 and day 101–105, showing that the number of aftershocks then increases temporarily in this volume.

Fig. 5(b) shows how the magnitude of the largest aftershock varies with time within the investigated day 91–95 cluster volume. During the first five days the magnitude of the largest aftershock is 5.8, taking place $\sim$2 min after the M 6.5 J17 main shock. This aftershock corresponds to the $M \sim 5$ event discussed by Vogfjord (2003) and its location is shown by the inverted triangle in Fig. 1. Due to the proximity in time to the main shock, it is difficult to assess whether it is the main shock or the M 5.8 aftershock that results in the large number of aftershocks in the investigated volume during the first five days. In the following 120 days, the maximum magnitude is scattered between $\sim$0.5–3 and is mostly lower than 2. Although there is a peak in the maximum magnitude (1.9) during day 91–95, it appears that there is no general correlation between a peak in the maximum magnitude (Fig. 5b) and a peak in the number of aftershocks (Fig. 5a). Moreover, maximum aftershock magnitudes of the same order does not, in general, correspond to similar values in the number of aftershocks. In the ETAS model we expect that aftershocks of a given magnitude always generates the same number of secondary aftershocks. It thus appears that secondary triggering and the ETAS model does not explain the observed rate increase during day 91–95 of the M 6.5 J17 aftershock sequence.

In Fig. 5(c) we show, how the proportion of aftershocks in the close vicinity of the aftershocks in the day 91–95 cluster varies with

time. To estimate this proportion, we divide the volume outlined by the dashed frames in Fig. 4 into smaller cubes of equal size and determine which of these cubes that are occupied by the aftershocks in the day 91–95 cluster. In five-day time steps through the *M* 6.5 J17 aftershock sequence, we then count and divide the number of aftershocks located within the cubes occupied by the day 91–95 cluster with the total number of *M* 6.5 J17 aftershocks in the investigated volume. In Fig. 5(c) we can see that the proportion of aftershocks in the cubes occupied by the day 91–95 off-fault cluster is below 20 per cent during the first 60 days. Then, this proportion is scattered between 10 and 50 per cent during the subsequent 60 days (except day 91–95, when it is 100 per cent as expected). The increase in the range of the scatter can be taken as an indication of more aftershock activity in the vicinity of the day 91–95 cluster.

We now consider the entire *M* 6.5 J17 aftershock region (Fig. 4), down to 12 km depth, when estimating how the proportion of aftershocks in close vicinity of the day 91–95 cluster varies with time. Utilizing a division of the entire volume into cubes of equal size, we estimate this proportion in the same way as for the proportion in Fig. 5(c). Fig. 5(d) shows that ∼35 per cent of the *M* 6.5 J17 aftershocks during day 91–95 occur in the cubes occupied by the day 91–95 off-fault cluster of aftershocks. This proportion of aftershocks represents a distinct peak in the distribution, as it otherwise is scattered below 20 per cent. This is an indication that the crustal volume of the off-fault aftershock cluster responsible for part of the rate increase in the *M* 6.5 J17 aftershock sequence becomes more active during day 91–95 after the main shock.

3.3 Summary of the spatiotemporal analysis of SISZ aftershock sequences

To summarize our analysis of the studied SISZ aftershock sequences, we have found the following.

(i) The aftershock sequences obey, in general, the Omori law for aftershocks describing the decay in the rate of aftershocks with time as $\mathrm{d}n/\mathrm{d}t = K/(c + t)^p$, where n is the number of aftershocks, K, c and p are empirical parameters, and t is the time since the main shock (Utsu 1961).

(ii) The duration of the initial period governed by an initially finite aftershock rate, measured by c in the Omori law, is significantly shorter for a smaller main shock than for a larger. A return of aftershock magnitudes to the long-term magnitude of completeness in a shorter time than measured by c indicates that the observed non-zero values of c may not only represent incomplete detection at short times after a main shock but may also reflect the physics of the aftershock process.

(iii) Significant deviations from the general power-law decay can be seen, with distinct and temporary drops in aftershock rate for all of the studied aftershock sequences. Following these drops, there is a distinct rate increase and the general power-law decay is resumed. For the *M* 4.5 S27 aftershock sequence, there is also a distinct and temporary increase in aftershock rate early in the sequence that is not precluded by a significant drop in rate.

(iv) The observed spatial distribution of *M* 4.5 S27, *M* 6.5 J17 and *M* 6.5 J21 aftershocks in dilatational and compressional quadrants of respective main shock is, with a confidence level well over 99 per cent, significantly different from a spatially uniform distribution. In the *M* 6.5 J17 and *M* 6.5 J21 sequences aftershocks of respective main shock fault zone are, in general, concentrated in the dilatational quadrants. In the *M* 4.5 S27 sequence most aftershocks are located in the vicinity of the likely main shock fault plane, with the majority in the dilatational quadrants.

(v) With time, the aftershocks in the *M* 4.5 S27, *M* 6.5 J17 and *M* 6.5 J21 sequences tend to cluster in the respective main shock fault zone, with little or no seismicity in the regions that are active during the initial, pre-power-law decay ($t < c$), period. The *M* 4.5 S27 aftershocks also exhibit an upward migration with time along the nodal plane that is the most likely main shock fault plane.

(vi) Aftershocks responsible for the distinct rate increase (point iii) form distinct spatial clusters. In the *M* 6.5 J17 and *M* 6.5 J21 sequences, such clusters occur both within respective main shock fault zone as well as off the fault zone. The aftershocks in the *M* 6.5 J17 and *M* 6.5 J21 off-fault clusters occur in the main shock dilatational quadrants, in parts of the crust becoming more seismically active than previously in the sequence. In the *M* 4.5 S27 sequence, the aftershock cluster responsible for the distinct rate increase also occur in the main shock dilatational quadrants, but in parts of the crust not previously seismically active. We find that this clustering in the dilatational quadrants is a robust observation with respect to errors in main shock strike in the *M* 6.5 J17 and *M* 6.5 J21 aftershock sequences but not in the *M* 4.5 S27 sequence.

(vii) For all of the studied aftershock sequences we find, with a confidence level over 95 per cent, that a spatially uniform aftershock distribution cannot produce the observed aftershock clustering in the dilatational quadrants of respective main shock during the distinct rate increases.

(viii) It appears to be no general correlation between large aftershock magnitudes and large number of aftershocks prior to and during the distinct rate increases in the *M* 6.5 J17 and *M* 6.5 J21 aftershock sequences. In the *M* 4.5 S27 aftershock sequence, however, we find a potential correlation of this kind. This implies that we may reject the ETAS model and secondary triggering as an explanation for the distinct rate increases in the *M* 6.5 J17 and *M* 6.5 J21 aftershock sequences but not in the *M* 4.5 S27 sequence.

4 MODELLING OF PORE PRESSURE-INDUCED SEISMICITY

In this paper we model seismicity induced by pore pressure diffusion processes following two hypothetical main shocks, one larger and one smaller. We also consider the effect of poroelastic adjustment of both stresses and pore pressures in the diffusion process. Our aim is not to resolve the complexity of the SISZ aftershock sequences studied but to investigate whether simple modelling can explain the general features of these sequences.

4.1 Modelling details and assumptions

4.1.1 Main shock fault models

The two hypothetical main shocks are modelled by buried, N–S striking vertical right-lateral strike-slip faults with a symmetric slip distribution as shown in Figs 6(a) and (b). In the two fault models the maximum slip is in the centre, 24 cm for the larger fault model and 2 cm for the smaller. The moment magnitude for the two main shocks is calculated by

$$M_w = \frac{2}{3}\log\left(G\sum_{i=1}^{N} A_i d_i\right) - 6.03, \tag{14}$$

where G is the shear modulus (30 GPa), A_i and d_i area and slip of patch i and N the number of patches. The moment magnitude M_w

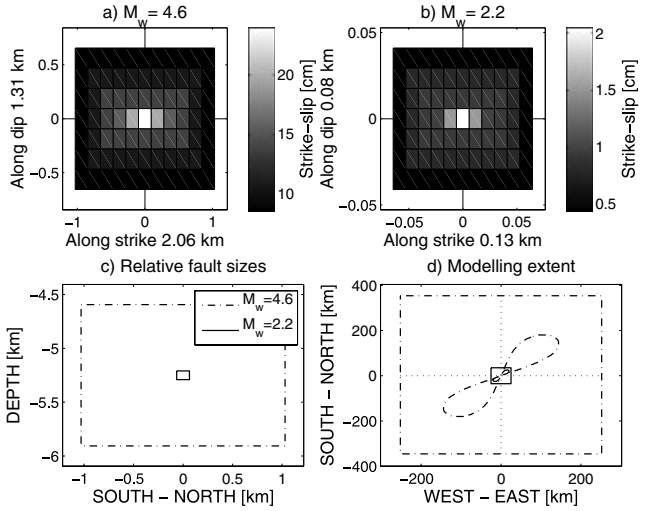

Figure 6. (a) and (b): slip distributions for the $M_w = 4.6$ and $M_w = 2.2$ fault models. (c) Vertical cross section showing the relative size of the two fault models. (d) Map view showing the modelling extent (solid black and dash-dotted rectangles) for the two fault models. Solid black ($M_w = 2.2$) and dash-dotted ($M_w = 4.6$) contours: maximum extent of potentially triggered points when modelling pore pressure diffusion with eq. (6).

is 4.6 for the larger main shock and 2.2 for the smaller. The fault models are placed in a cartesian coordinate system. Fig. 6(c) shows the relative dimensions of the two faults, both having the same midpoint at 5.25 km depth. The vertical faults have dimensions ($L \times W$) of 2.0 × 1.3 km ($M_w = 4.6$) and 129 × 82 m ($M_w = 2.2$).

4.1.2 Background stress state and regional pore pressure

In our modelling, we assume that the background stress state of the crust is strike-slip and that optimally oriented faults are on the point of failure according to the Mohr-Coulomb failure criterion. We assume that the principal stresses σ_1^b and σ_3^b are both horizontal and that the intermediate principal stress σ_2^b is vertical and equal to the weight of the overburden, that is,

$$\sigma_2^b = -\rho_c g Z, \tag{16}$$

where ρ_c is the density of the crust and the depth Z is considered negative. The direction of σ_1^b is assumed to be N30° E, consistent with N–S striking faults if the frictional coefficient μ is equal to 0.6 (Byerlee 1978). Although our modelling takes place in a hypothetical crust, this direction is consistent with the results of Lund & Slunga (1999) and Bergerat & Angelier (2000) for Iceland.

Given σ_1^b, the value of σ_3^b on optimally oriented faults on the point of failure can be calculated from the Mohr-Coulomb failure criterion (when $\tau_0 = 0$) as

$$\sigma_3^b = \left(\sigma_1^b - P_{\text{reg}}\right)\left[(\mu^2+1)^{1/2} - \mu\right]^2 + P_{\text{reg}}, \tag{17}$$

where P_{reg} is the regional pore pressure. P_{reg} is assumed to be hydrostatic, that is,

$$P_{\text{reg}} = -\rho_w g Z, \tag{18}$$

where ρ_w is the density of water. We now relate the magnitude of σ_2^b to the magnitude of σ_1^b and σ_3^b through the ratio Φ (Angelier *et al.* 1982):

$$\Phi = \frac{\sigma_2^b - \sigma_3^b}{\sigma_1^b - \sigma_3^b}. \tag{19}$$

Using eq. (17), eq. (19) can be rewritten to yield an expression for σ_1^b in terms of σ_2^b, Φ, P_{reg} and μ.

$$\sigma_1^b = \frac{\sigma_b^2 - P_{\text{reg}}}{\Phi - (\Phi - 1)\left[(\mu^2+1)^{1/2} - \mu\right]^2} + P_{\text{reg}}. \tag{20}$$

Given the depth Z, the stress ratio Φ and the Mohr-Coulomb friction coefficient μ the background state of stress can now be calculated from eqs (16), (18), (20) and (17). Here we use $\Phi = 0.5$, implying that σ_2^b is located halfway between σ_1^b and $\sigma^b{}_3$. The results and conclusions in this paper are robust with respect to the value of Φ as its effect on the critical pore pressures and the associated pore pressure triggering is insignificant in our modelling.

4.1.3 Solution of the pore pressure and poroelastic diffusion equations

To solve the pore pressure and poroelastic diffusion equations (eqs 6 and 8), we apply a 3-D finite difference scheme on two regular grids, one for the $M_w = 2.2$ main shock and one for the $M_w = 4.6$ main shock. The dimensions of each grid are selected based on eq. (14) and the maximum spatial extent of potential triggering (see Section 2.4) illustrated by the contours in Fig. 6(d). This figure clearly demonstrates that the crustal regime affected by the $M_w = 2.2$ is much smaller than the regime affected by the $M_w = 4.6$ earthquake. For the two grids we thus select the modelling extent outlined in Fig. 6(d): 50 km (E) × 70 km (N) × 16 km (Z) with 0.2 km grid spacing for the $M_w = 2.2$ event (solid rectangle) and 500 km (E) × 700 km (N) × 16 km (Z) with 2 km grid spacing for the $M_w = 4.6$ event (dash-dotted rectangle). In the finite difference scheme we use a time step $\Delta t = 10$ s and apply boundary conditions as described in Lindman *et al.* (2006).

Given the elastic deformation associated with the $M_w = 2.2$ and $M_w = 4.6$ main shocks, the corresponding diffusion processes are initiated by calculating coseismic pore pressure and stress changes (eqs 4 and 5) in the $M_w = 2.2$ and $M_w = 4.6$ grids, respectively. For the $M_w = 4.6$ fault model, we also use eq. (10) and the coseismic changes in pore pressure given by eq. (4) to calculate the values of $\Delta\sigma_{kk}$ to use as starting values in the term $\Delta\sigma_{kk} - \frac{3}{B}\Delta P$ of the poroelastic diffusion equation.

The finite difference solution of the pore pressure diffusion equation (eq. 6) yields $\Delta P(x, y, z, t)$, that is, how the pore pressure perturbation varies with time at each of the gridpoints. When modelling induced seismicity with the pore pressure diffusion equation, we only consider the effect of the diffusing pore pressure transients. To investigate the relationship between pore pressure-induced seismicity and the magnitude of the main shock initiating the diffusion process, we use the same value of D (=15 m^2 s^{-1}) for both main shocks.

When solving the poroelastic diffusion equation (eq. 8) we use $c_m = 15$ m^2 s^{-1} to allow direct comparison with the modelling using the pore pressure diffusion equation (eq. 6). The finite difference solution of the poroelastic diffusion equation yields the temporal variation in $\Delta\sigma_{kk} - \frac{3}{B}\Delta P$. The condition given by eq. (10) can then be used to determine the temporal variation in $\Delta\sigma_{kk}$ and ΔP themselves, respectively. However, to determine the temporal variation in the individual tensor elements of the stress perturbation ($\Delta\sigma_{ij}$) eq. (11) needs to be solved repeatedly, for each new value of $\Delta\sigma_{kk}$ and ΔP. Solving eq. (11) would be computationally prohibitive due to the large region where the diffusion process is modelled. Knowing $\Delta\sigma_{kk}(x, y, z, t)$, we therefore take the following steps to mimic

the behaviour of a time-varying stress perturbation satisfying force equilibrium and strain and stress compatibility equations.

(i) We calculate stresses induced by an earthquake using eq. (5) and assume that the relative proportions between all elements of the corresponding stress tensor will remain the same during the diffusion process. Thus, the stress perturbation tensor at time t_{i+1} is a scaled version of the tensor at time t_i.

(ii) We require the stress perturbation tensor to satisfy eq. (10) at each time step. As the coseismically induced stress perturbation (eq. 5) satisfies $\Delta\sigma_{kk} = (3/B)\Delta P_{\rm ind}$ we calculate a scaling factor

$$Q_0 = \frac{2(\nu_u - \nu)}{(1-\nu)(1+\nu_u)}, \tag{21}$$

and scale all of the elements of the coseismically induced stress perturbation tensor with this factor, that is,

$$\Delta\sigma_{ij}(t_0) = Q_0 \Delta\sigma_{ij}^{\rm ind}. \tag{22}$$

With this scaling, the mean stress of the resulting tensor, $\Delta\sigma_{kk}(t_0)$, satisfies eq. (10). We have checked how well eq. (11) is satisfied with the rescaled stress tensor. By evaluating the left-hand side of eq. (11) numerically at two locations, one close to the main shock fault zone and one at greater distance, we find that the difference from zero is in the order of 10^{-2}. We thus conclude that the rescaling provides a reasonable approximation of a stress tensor satisfying force equilibrium and strain and stress compatibility equations.

(iii) At a time step t_n, $n = 1, 2, 3, ..., N$, we solve for $\Delta P\,(t_n)$ and $\Delta\sigma_{kk}\,(t_n)$ using the value of $\Delta\sigma_{kk} - \frac{3}{B}\Delta P$ (obtained from the solution of the poroelastic diffusion equation) and eq. (10). We then calculate the stress perturbation tensor at time t_n from

$$Q_n = \frac{\Delta\sigma_{kk}\,(t_n)}{\Delta\sigma_{kk}\,(t_{n-1})}, \tag{23}$$

$$\Delta\sigma_{ij}\,(t_n) = Q_n \Delta\sigma_{ij}\,(t_{n-1})\,. \tag{24}$$

4.1.4 Timing of triggering by pore pressure changes

As discussed in Section 2.4 the critical pore pressure does not change with time when modelling the main shock-initiated diffusion process with the pore pressure diffusion equation (eq. 6). During a given time step (i) in the finite difference scheme triggering is then considered to have taken place for the gridpoints where

$$P_{\rm reg} + \Delta P(t_i) \geq P_{\rm crit}^{\rm pert}\,, \tag{25}$$

where $P_{\rm reg}$ is the regional pore pressure, $\Delta P(t_i)$ the diffusing pore pressure transient at time step number i and $P_{\rm crit}^{\rm pert}$ the critical pore pressure. For the triggered point(s) the triggering time is found by determining when a linear interpolation of $P_{\rm reg} + \Delta P(t)$ between time step $i-1$ and i equals $P_{\rm crit}^{\rm pert}$.

When modelling the diffusion process with the poroelastic diffusion equation (eq. 8), however, the background state of stress is modified at each time step with the time-dependent stress perturbation given by eq. (24). Having determined the principal stresses of this modified stress state, eq. (13) gives the critical pore pressure (at the given time step) necessary for failure. During a given time step (i) triggering is then considered to have taken place for the gridpoints where

$$P_{\rm reg} + \Delta P(t_i) \geq P_{\rm crit}^{\rm pert}(t_i), \tag{26}$$

where $P_{\rm reg}$ is the regional pore pressure, $\Delta P(t_i)$ the pore pressure transient at time step number i and $P_{\rm crit}^{\rm pert}\,(t_i)$ the perturbed critical pore pressure at time step number i. For the triggered points the triggering time is found from a linear interpolation of $P_{\rm reg} + \Delta P(t)$ and $P_{\rm crit}^{\rm pert}\,(t)$ between time step $i-1$ and i.

In the diffusion processes that we have modelled in this paper, we do not allow for triggering of gridpoints at the surface ($Z = 0$) and we only allow each point to be triggered once. We also consider each triggered gridpoint to represent a cubic volume in which earthquakes can be triggered by the diffusion process. For the $M_w = 2.2$ and $M_w = 4.6$ grids, the sizes of the corresponding volumes are $0.2 \times 0.2 \times 0.2\,{\rm km}^3$ and $2 \times 2 \times 2\,{\rm km}^3$, respectively. An estimate of the temporal variation in the volumetric rate of triggering can thus be obtained by multiplying the temporal distribution of the obtained triggering time-series with the associated cube size.

4.2 Modelling results

4.2.1 Temporal variation in pore pressure triggering rate

In the modelled $M_w = 2.2$ and $M_w = 4.6$ diffusion processes Fig. 7(a) shows that the initially finite triggering rate and subsequent power-law decay is in agreement with Omori's law with a non-zero value of c. Comparing the triggering in the two diffusion processes, we can see that the duration of the pre-power-law decay period is shorter for the $M_w = 2.2$ main shock than for the $M_w = 4.6$ main shock. Moreover, Fig. 7(a) also shows that crustal volumes are enabled for triggering earlier in the $M_w = 2.2$ case than in the $M_w = 4.6$ case and that the triggering rate begins to fall below the

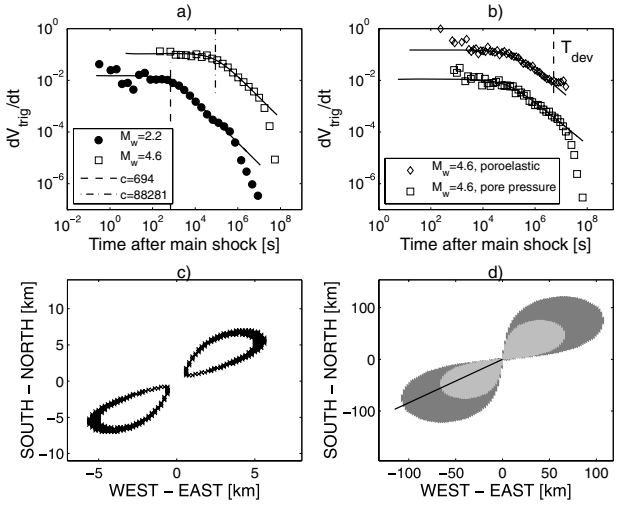

Figure 7. (a) Volumetric triggering rate versus time, pore pressure diffusion (eq. 6). Solid circles: diffusion initiated by the $M_w = 2.2$ main shock. Open squares: diffusion initiated by the $M_w = 4.6$ main shock. Solid curves: the Omori law with parameters $K = 410.7$, $c = 694$, $p = 0.82$ ($M_w = 2.2$) and $K = 164.7$, $c = 88281$, $p = 0.82$ ($M_w = 4.6$). Dashed and dash-dotted vertical lines: indicates the respective values of c. (b) Volumetric triggering rate versus time, $M_w = 4.6$ diffusion process. Open squares: pore pressure diffusion equation (eq. 6). Open diamonds: poroelastic diffusion equation (eq. 8). Solid curves: the Omori law. Dashed vertical line: indicates the timing, $T_{\rm dev}$, of a deviation from the Omori law in the poroelastic diffusion process. (c) Slice through triggered volume at 4 km depth in the $M_w = 2.2$ pore pressure diffusion process (eq. 6). (d) Slice through triggered volume at 4 km depth in the $M_w = 4.6$ poroelastic diffusion process (eq. 8). Dark grey: triggering takes place before $T_{\rm dev}$ (see b). Light grey: triggering takes place after $T_{\rm dev}$ (see b). Solid line: a profile along which quantities related to the $M_w = 4.6$ poroelastic diffusion process is shown in Fig. 8.

Omori law at large times, indicating that pore pressure triggering is limited in time.

The difference between using the pore pressure and the poroelastic diffusion equation in our modelling of the $M_w = 4.6$ diffusion process is shown in Fig. 7(b). Instead of a fall in the triggering rate below the Omori law at large times poroelastic diffusion results in distinct hump with a temporary increase in triggering rate. The origin of this hump will be discussed in Section 4.2.3.

4.2.2 Spatial extent of pore pressure triggering

A slice through the triggering volume at 4 km depth is shown in Fig. 7(c) for the $M_w = 2.2$ pore pressure diffusion process and in Fig. 7(d) for the $M_w = 4.6$ poroelastic diffusion process. In both cases, triggering takes place within the dilatational quadrants of the right lateral faults, where pore pressures decrease coseismically and increase post-seismically. Comparing the two plots, it can be seen that the crustal volume of pore pressure triggering is larger for a larger main shock than for a smaller. Moreover, pore pressure diffusion results in an internal region void of triggering (Fig. 7c) while poroelastic diffusion results in an corresponding region (Fig. 7d) where triggering is active during the hump and rate increase at large times in Fig. 7(b).

4.2.3 Spatiotemporal evolution of the modelled pore pressure diffusion processes

In Fig. 8 we present plots of some pore pressure diffusion-related quantities along sections of a profile at 4 km depth, cutting through the triggering volume and passing through the midpoint of the $M_w = 4.6$ fault trace at this depth (see Fig. 7d). Fig. 8(a) shows that the magnitude of coseismic and cumulative post-seismic changes in pore pressure at different times after the main shock behave in a non-linear way as the fault zone is approached, with the near fault zone being the most significantly affected. Moreover, the cumulative post-seismic pore pressure changes after 147 days are visually indistinguishable from the cumulative changes after 14 days. In the pore pressure diffusion process strong heterogenities and spatial pore pressure gradients are reduced with time, implying, as demonstrated in Fig. 8(a), that post-seismic changes in pore pressure will slow down with time.

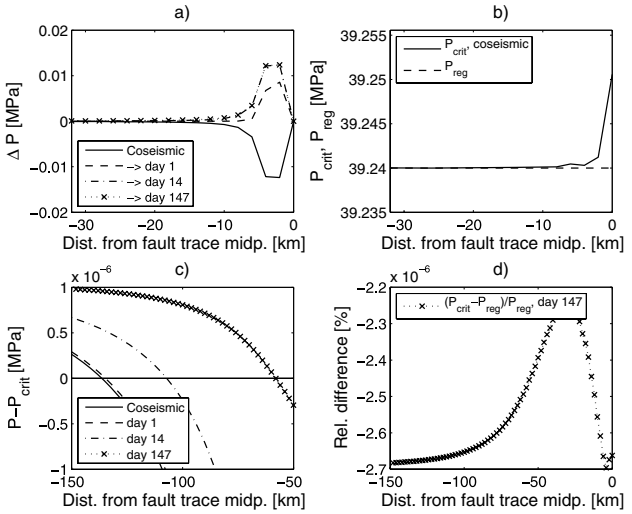

Figure 8. Quantities related to the $M_w = 4.6$ poroelastic diffusion process plotted along sections of the profile (at 4 km depth) in Fig. 7(d). (a) Coseismic and cumulative post-seismic change in pore pressure at different times. (b) Initial value of P_{crit} (solid curve). The regional (hydrostatic) pore pressure is shown for reference (dashed curve). (c) $P - P_{\text{crit}}$ at different times in the diffusion process. P is the sum of the diffusing pore pressure transient and the regional pore pressure. (d) Relative difference between P_{crit} and the regional pore pressure P_{reg} 147 days after the initiation of the diffusion process.

Considering the variation in critical pore pressure (required for triggering) along the profile, Fig. 8(b) shows that the initial, coseismic, critical pore pressure increases in a non-linear fashion and eventually becomes larger than the regional, undisturbed, critical pore pressure P_{reg} as the fault zone is approached. In the pore pressure diffusion process triggering migrates towards the main shock fault zone with time, and the non-linear increase in the critical pore pressure implies a transition into a power-law decay of the volumetric triggering rate. Pore pressure triggering, however, cannot take place as long as the critical pore pressure is larger than the regional pore pressure. This explains the internal regions void of triggering in Fig. 7(c), and the rapid fall in triggering rate below the Omori law power-law decay at large times in Fig. 7(a).

In the poroelastic diffusion process the critical pore pressure (required for triggering) varies with time. In Fig. 8(c) the difference between the total and the critical pore pressure (i.e. $P - P_{\text{crit}}$) at different times is plotted along a section of the profile in Fig. 7(d). A negative difference implies that the total pore pressure is not large enough to enable triggering. Fig. 8(c) shows that the distance to the fault zone from the point where $P - P_{\text{crit}}$ changes from positive to negative decreases with time. This implies that crustal volumes closer and closer to the main shock fault zone will, successively, become enabled for triggering during the poroelastic diffusion process.

Fig. 8(d) shows that the critical pore pressure is lower than the regional pore pressure along the entire profile 147 days after the $M_w = 4.6$ main shock, implying that the poroelastic diffusion process may now cause triggering also close to the fault zone. With time, the reduction of the critical pore pressure will, successively, be faster and faster in the poroelastic diffusion process. Although the rate of pore pressure recovery slows down with time this implies that the volumetric triggering rate may increase temporarily, as shown by the hump in Fig. 7(b), when the critical pore pressure has dropped below the regional pore pressure.

5 INTERPRETATION OF SISZ AFTERSHOCK SEQUENCES IN TERMS OF PORE PRESSURE DIFFUSION

Both the studied SISZ aftershock sequences and the volumetric pore pressure triggering rate in our modelling exhibit general Omori law behaviour. We know that earthquakes causes bulk volume deformation that may be reflected in coseismic reduction of pore pressures in dilatational quadrants and increases in compressional quadrants. We also know that pore pressures reduces shear failure stresses and that pore pressure triggering effects must be present, to some extent, during main shock-initiated pore pressure diffusion processes in the post-seismic period. In this section we will therefore suggest an interpretation for how post-seismic pore pressure diffusion may yield (1) an initially finite aftershock rate and a pre-power-law decay period, (2) a subsequent power-law decay in the rate and clustering of aftershocks with time in the main shock fault zone and (3) distinct rate drops and rate increases during the Omori power-law decay.

5.1 The initially finite rate of aftershocks and a pre-power-law decay period

In an aftershock sequence obeying the Omori law, an initially finite aftershock rate (i.e. a non-zero value of c) implies that there is a temporal delay between the main shock and the first aftershock that occurs. In our modelling of main shock-initiated pore pressure diffusion it takes some time for pore pressures to recover and enable triggering in the crustal volume affected by the main shock. We thus interpret the origin of an initially finite aftershock rate in the studied SISZ aftershock sequences as due to a temporal triggering delay in main shock-initiated pore pressure diffusion processes.

We now turn to the origin of the initial pre-power-law decay period in the studied SISZ aftershock sequences. The coseismic influence of a main shock on stresses and pore pressures in the crust is, in general, largest in the vicinity of the main shock fault zone and dies off in a non-linear fashion with increasing distance from the fault zone. We interpret the origin of the initial pre-power-law decay period within the SISZ as due to this non-linear influence of main shocks on the surrounding crust, implying that pore pressure recovery needs significantly less time to overcome failure thresholds away from the main shock fault zone than in its vicinity. When approaching the main shock fault zone the non-linear increase in the coseismic influence on the crust implies an upper limit for the duration of the pre-power-law decay period which, essentially, is governed by the magnitude of the main shock. A larger main shock influences the surrounding crust to a larger degree than a smaller, both in terms of the spatial extent of the affected volume and in terms of the magnitude of the coseismic stress and pore pressure changes. Therefore, the associated pore pressure diffusion processes needs longer time to enable triggering, increasing both the duration of the pre-power-law decay period and the total time period of pore pressure triggering.

When modelling pore pressure diffusion processes associated with different types of main shock faulting and permeabilities, Gavrilenko (2005) found the initial pre-power-law decay period to be sustained longer the lower the permeability. From the pore pressure or poroelastic diffusion equations (eq. 6 or 8) we can see that a lower permeability implies a lower rate of pore pressure recovery. This implies that the pre-power-law decay period can be sustained longer, as pore pressure recovery will take a longer time with a lower permeability. We conclude that the duration of the initial pre-power-law decay period is related both to the permeability of the medium and to the magnitude and fault slip distribution of the main shock.

5.2 The power-law decay in the rate of aftershocks and clustering of aftershocks with time in the main shock fault zone

During the power-law decay in aftershock rate, our time stepping through the spatial distribution of the M 4.5 S27, M 6.5 J17 and M 6.5 J21 aftershocks shows that they tend to, in general, cluster in the vicinity of the respective main shock fault zone with time. This is consistent with the results of our modelling, where the main shock initiated diffusion process successively, at a rate that decays as a power law with time, enables triggering in crustal volumes closer and closer to the main shock fault zone. Based on our discussion in Section 4.2.3 we thus interpret the origin of the power-law decay in aftershock rate and the increased clustering in main shock fault zones with time as a combination of a non-linear increase in critical pore pressures when approaching the fault zone and a slowing down of the pore pressure recovery with time in the diffusion process.

5.3 Distinct rate drops and rate increases during the Omori power-law decay

Our modelling demonstrates that allowing poroelastic adjustment of stresses activates crustal volumes where triggering was inhibited previously, and that this results in an upward deviation from the Omori law power-law decay in volumetric triggering rate (i.e. a rate increase). Such an activation is consistent with the results of Piombo *et al.* (2005), showing that poroelastic adjustment can result in a change from inhibitation to promotion of induced seismicity during the diffusion process. If we do not allow for poroelastic adjustment of stresses, however, the volumetric triggering rate falls rapidly as triggering in crustal volumes closer to the main shock fault zones remains inhibited.

The modelling in this paper is not intended to capture the complexities of the studied aftershock sequences in the SISZ. We note that the character and timing of the modelled rate increase when taking poroelasticity into account does not resemble the distinct rate increases in the studied aftershock sequences. This may be explained by the simplicity of our model and the fact that we obtain a volumetric triggering rate rather than an event triggering rate. From the modelling we do not know the number of aftershocks that may actually be triggered during a main shock-initiated diffusion process. We know, however, that pore pressure diffusion and poroelastic effects must be present and influence the studied aftershock sequences in the SISZ to some extent.

It is interesting to note that the SISZ aftershocks associated with the distinct rate increases do cluster within dilatational parts of the crust either being previously inactive or becoming more seismically active than earlier in the sequence. For the studied aftershock sequences this clustering is significantly different than that produced by aftershocks uniformly distributed over the main shock focal sphere. This clustering is also a robust observation with respect to errors in main shock strike in the M 6.5 J17 and M 6.5 J21 aftershock sequences. Except for the clustering off the main shock fault zone during the distinct rate increases in these two sequences we also observe increased clustering with time in the main shock fault zones. This observation is in agreement with our modelling, where the pore pressure diffusion process successively enables triggering closer and closer to the main shock fault zone. We thus consider it motivated to interpret also the deviations from the Omori law in terms of main shock-initiated pore pressure diffusion.

Based on the modelling and data analysis in this paper we suggest that a possible origin of the distinct deviations from the Omori law (rate drops and rate increases) in the studied SISZ aftershock sequences is a combination of inhibitation and activation in a poroelastic diffusion process and crustal heterogenities (e.g. stress state, frictional properties, permeabilities, etc.). In a more complex pore pressure diffusion model it may thus be possible that the rate increases due to the poroelastic effect resembles both the timing and character of the observed rate increases in the studied SISZ aftershock sequences.

6 DISCUSSION

In seismogenic zones there is, without a doubt, a complex relationship between the properties of the Earth's crust and the occurrence of earthquakes. Pre-existing fractures of various orientations and

heterogenities in mechanical properties, existence of pore fluids, permeabilities and the state of stress are some factors that have an influence on earthquake occurrence. The empirically well-established applicability of the Omori law for aftershocks in seismogenic zones of different character, however, suggests that underlying physical processes may govern this behaviour, rather than only the complexities in the state of the Earth's crust. In the previous section we interpreted the characteristic features of the studied SISZ aftershock sequences in terms of main shock-initiated pore pressure diffusion processes. We will now discuss alternative interpretations for two of these features, namely the initially finite rate of aftershocks (and the associated pre-power-law decay period) and the distinct and temporary deviations from the Omori law power-law decay.

6.1 Alternative interpretations for the initially finite aftershock rate and the pre-power-law decay period

Alternative models that can explain an initially finite rate of aftershocks include dynamically propagating cracks (e.g. Yamashita & Knopoff 1987; Shaw 1993; Kanamori & Brodsky 2004) or rate- and state-dependent frictional slip on faults (e.g. Dieterich 1994; Kanamori & Brodsky 2004). In these models a static stress change perturbs the loading rate and increases the sliding speed on faults, thus shortening the time to failure and yielding a rate of aftershocks obeying the Omori law (Kanamori & Brodsky 2004). A finite stress change implies an initially finite aftershock rate (as the time to failure of the first aftershock is not reduced to zero) and a pre-power-law decay period in the rate of aftershocks, that is, a non-zero value of the Omori law parameter c. However, as the magnitude of the static stress change goes to infinity the occurrence time of the first aftershock goes to zero, the initial aftershock rate goes to infinity and the subsequent rate goes to a pure power-law decay with time (i.e. the Omori law parameter c goes to a zero value). Under the assumption of a constant background stressing rate (due to e.g. plate motions) this implies that the larger the stress change, that is, the larger the main shock, the shorter is the duration of the pre-power-law decay period (Dieterich 1994; Kanamori & Brodsky 2004).

In contradiction to our pore pressure diffusion model, rate and state friction and dynamically propagating crack models thus predict that the duration of the pre-power-law decay period in the rate of aftershocks is inversely related to the magnitude of the main shock. Moreover, the assumption of a constant stressing rate in these models implies that aftershock sequence duration is constant and independent of the magnitude of the stress change, that is, the main shock magnitude. Our pore pressure diffusion model on the other hand predicts, as observed in real aftershock sequences, an aftershock sequence duration which increases with increasing main shock magnitude. Another feature of rate and state friction and dynamically propagating crack models is also that they only consider the effect of a static stress change on a fault population, where there is no spatial interaction within the crust. A pore pressure diffusion model, however, considers both the effect of main shock-induced stress changes and spatial interaction within the crust through the diffusion process initiated by the main shock.

It has been proposed that the value of c in the Omori law reflects the main shock faulting style and the crustal state of stress, with the lowest c values for thrust events (large differential stress), intermediate for strike-slip events (intermediate differential stress) and the largest for normal faulting events (low differential stress) (Narteau *et al.* 2009). In this study, however, we find that the normal faulting style M 3.2 F28 and M 4.5 S27 main shocks yields significantly smaller c values of the associated aftershock sequences than the strike-slip M 6.5 J17 and M 6.5 J21 main shocks. This increase in c value with main shock magnitude may, as discussed in Section 3.1.3, not only reflect incompleteness artefacts but also the physics of the aftershock process. It thus appears that the proposed stress state dependency of the Omori law c value (Narteau *et al.* 2009) may not be applicable to the studied SISZ aftershock sequences.

6.2 Alternative interpretations for the distinct deviations from the Omori law

In the studied aftershock sequences from the SISZ we have pointed out deviations from the Omori law power-law decay (Fig. 2). As discussed in Section 3.1.2 we can interpret these deviations in terms of secondary triggering behaviour and the ETAS model of seismicity (Ogata 1988). We find, however, that a general correlation between the distinct rate increases and larger magnitudes of preceding aftershocks is lacking in two of the three studied aftershock sequences (the M 6.5 J17 and M 6.5 J21 sequences). Although the ETAS model may explain the observed deviations from the Omori law in the M 4.5 S27 sequence it appears that we cannot use this model as a general explanation for these features in all of the studied SISZ aftershock sequences.

Other processes that may have an influence on the occurrence of aftershocks are viscoelastic relaxation of the lower crust and upper mantle (e.g. Deng *et al.* 1999; Freed & Lin 2001) and/or afterslip (e.g. Perfettini & Avouac 2004; Hsu *et al.* 2006) on or adjacent to the main shock rupture. Following the M 6.5 J17 and the M 6.5 J21 earthquakes, geodetic data from the SISZ have revealed a deformation transient with a characteristic timescale of about 1 yr, that can be explained by either viscoelastic relaxation of the lower crust and upper mantle or afterslip on narrow shear zones extending from 8–14 km depth below the M 6.5 J17 and M 6.5 J21 ruptures (Árnadóttir *et al.* 2005). It appears unlikely, however, that afterslip is the mechanism as the location of maximum afterslip obtained by Árnadóttir *et al.* (2005) does not correlate well with the aftershocks occurring within the fault zones during the rate increase. Afterslip limited only to shear zones below the main shock rupture zones also appears unlikely as aftershocks during the rate increase also occur outside the main shock fault zone in the M 6.5 J17 and M 6.5 J21 sequences. In the M 4.5 S27 sequence the upward migration of aftershocks during the two periods of rate increase also appear inconsistent with possible afterslip taking place downdip of the hypocentral region.

Based on analysis of post-seismic deformation measured by satellite radar interferometry Jónsson (2008) suggests that the slow deformation transient following the 2000 June earthquakes in Iceland was most likely driven by viscoelastic relaxation. We now use the timing of the distinct aftershock rate increases in the studied SISZ sequences to estimate the required viscosities if post-seismic viscoelastic relaxation of the lower crust is the cause. Assuming Newtonian viscosity, and equating the viscous deformation of the lower crust with the deformation of the elastic upper crust caused by the viscous increase in stress, the viscosity can be estimated from $\eta = t\ 2G/f$, where t is the time of the rate increase, G the shear modulus of the upper crust and f the fraction of the coseismic stress change induced in the upper crust by the viscous relaxation.

If we assume that the rate increases are caused by a viscous shear stress increase of 10^4 Pa (0.1 bar), the fraction f is, with a 10 km thick upper crust, approximately $1/30$ for a M 6.5 earthquake and $1/10$ for a M 4.5 earthquake. Using a shear modulus for the upper crust

of 30 GPa and the boundaries of the time intervals in Figs 2(a)–(c) exhibiting distinct rate increases, we estimate viscosities of the order of 6.5–9.3 $\times$ 10^{16} and 5.4–7.9 $\times$ 10^{17} Pas (the *M* 4.5 S27 sequence), 8.9 $\times$ 10^{18} $-$ 1.8 $\times$ 10^{19} Pas (the *M* 6.5 J17 sequence) and 1.1 $\times$ 10^{19} $-$ 1.8 $\times$ 10^{19} Pas (the *M* 6.5 J21 sequence), respectively. As the *M* 6.5 J17 and *M* 6.5 J21 viscosities lie in the range estimated for Iceland, (1.0 $\times$ 10^{18} $-$ 5.0 $\times$ 10^{19} Sigmundsson 1991; Sigmundsson & Einarsson 1992; Pollitz & Sacks 1996; Árnadóttir *et al.* 2009) we cannot rule out viscoelastic relaxation as the cause of the distinct rate increases in the *M* 6.5 J17 and *M* 6.5 J21 aftershock sequences. In the *M* 4.5 S27 sequence, however, the rate increases occur as early as 1.25–1.8 and 10.5–15.2 days after the main shock, and the estimated viscosities are too low. Viscoelastic relaxation, therefore, does not appear to be a general mechanism underlying distinct rate increases in the studied SISZ aftershock sequences.

7 CONCLUSIONS

To summarize, we conclude that main shock initiated pore pressure diffusion and poroelastic stress relaxation provide a physical model that have the potential to explain characteristic features of aftershock sequences in the SISZ, that is, an initially finite aftershock rate, a pre-power-law decay period, whose duration is larger following a larger main shock, and a subsequent power-law decay that is interrupted by distinct and temporary deviations in terms of rate increases and decreases. We find that the observed main shock magnitude dependent duration of the initial pre-power-law decay period is inconsistent with rate and state friction and dynamically propagating crack models as well as a proposed dependence on the crustal state of stress, and that either secondary triggering in the ETAS model, afterslip or viscoelastic relaxation do not provide a general explanation for the observed deviations from the power-law decay in aftershock rate in the studied sequences.

We consider the ability and potential of pore pressure diffusion and poroelastic stress adjustment to capture the characteristic features of aftershock sequences in the SISZ as promising for our understanding of the physics of the aftershock process. In particular, we consider that the coupling between the pre-power-law decay period and main shock magnitude on one hand and the power-law decay in aftershock rate and increased clustering with time in main shock fault zones on the other hand constitute strong evidence for pore pressure effects in aftershock triggering within the SISZ. We recommend that poroelastic stress adjustment is taken into account in modelling of aftershock triggering associated with main shock-initiated pore pressure diffusion.

ACKNOWLEDGMENTS

We would like to thank the Icelandic Meteorological Office for supplying the data used in this study. Suggestions and comments by I. Main and an anonymous reviewer improved the quality of this paper and are highly appreciated.

REFERENCES

Angelier, J., Tarantola, A., Valette, B. & Manoussis, S., 1982. Inversion of field data in fault tectonics to obtain the regional stress, I, single phase fault populations: a new method of computing the stress tensor, *Geophys. J. R. astr. Soc.*, **69**(3), 607–621.

Antonioli, A., Belardinelli, M.E., Bizzari, A. & Vogfjord, K.S., 2006. Evidence of instantaneous dynamic triggering during the seismic sequence of year 2000 in south Iceland, *J. geophys. Res.,* **111**(B3), B03302, doi:10.1029/2005JB003935.

Árnadóttir, T., Jónsson, S., Pollitz, F.F., Jiang, W. & Feigl, K.L., 2005. Postseismic deformation following the June 2000 earthquake sequence in the south Iceland seismic zone, *J. geophys. Res.,* **110**(B12), B12308, doi:10.1029/2005JB003701.

Árnadóttir, T., Lund, B., Jiang, W., Geirsson, H., Björnsson, H., Einarsson, P. & Sigurdsson, T., 2009. Glacial rebound and plate spreading: results from the first countrywide GPS observations in Iceland, *Geophys. J. Int.*, **177,** 691–716.

Beck, J.L., 1976. Weight-induced stresses and the recent seismicity at Lake Oroville, California, *Bull. seism. Soc. Am.*, **66**(4), 1121–1131.

Bell, M.L. & Nur, A., 1978. Strength changes due to reservoir-induced pore pressure and stresses and application to Lake Oroville, *J. geophys. Res.*, **83**(B9), 4469–4483.

Bergerat, F. & Angelier, J., 2000. The South Iceland Seismic Zone: tectonic and seismotectonic analyses revealing the evolution from rifting to transform motion, *J. Geodyn.,* **29**(3–5), 211–231.

Björnsson, G., Flovenz, O., Saemundsson, G. & Einarsson, K., 2001. Pressure changes in Icelandic geothermal reservoirs associated with two large earthquakes in June 2000, in *Proc. 26th Workshop on Geothermal Reservoir Engineering SGP-TR-16,* pp. 327–334, Stanford University, Stanford.

Bosl, W.J. & Nur, A., 2002. Aftershocks and pore fluid diffusion following the 1992 Landers earthquake, *J. geophys. Res.,* **107**(B12), 2366, doi:10.1029/2001JB000155.

Brace, W.F. & Kohlstedt, D.L., 1980. Limits on lithospheric stress imposed by laboratory experiments, *J. geophys. Res.*, **85**(B11), 6248–6252.

Byerlee, J., 1978. Friction of rocks, *Pure appl. Geophys.*, **116**(4–5), 615–626.

Deng, J.S., Hudnut, K., Gurnis, M. & Hauksson, E., 1999. Stress loading from viscous flow in the lower crust and triggering of aftershocks following the 1994 Northridge California, earthquake, *Geophys. Res. Lett.*, **26**(21), 3209–3212.

Dieterich, J.H., 1994. A constitutive law for rate of earthquake production and its application to earthquake clustering, *J. geophys. Res.*, **99**(B2), 2601–2618.

Einarsson, P., 1991. Earthquakes and present-day tectonism in Iceland, *Tectonophysics*, **189**(1–4), 261–279.

Enescu, B., Mori, J. & Miyazawa, M., 2007. Quantifying early aftershock activity of the 2004 mid-Niigata Prefecture earthquake (Mw6.6), *J. geophys. Res.,* **112**(B4), B04310, doi:10.1029/2006JB004629.

Freed, A.M. & Lin, J., 2001. Delayed triggering of the 1999 Hector Mine earthquake by viscoelastic stress transfer, *Nature*, **411**(6834), 180–183.

Gavrilenko, P., 2005. Hydromechanical coupling in response to earthquakes: on the possible consequences for aftershocks, *Geophys. J. Int.*, **161**(1), 113–129.

Greenhough, J. & Main, I.G., 2008. A Poisson model for earthquake frequency uncertainties in seismic hazard analysis, *Geophys. Res. Lett.*, **35**(19), L19313, doi:10.1029/2008GL035353.

Gutenberg, B. & Richter, C.F., 1944. Frequency of earthquakes in California, *Bull. seism. Soc. Am.*, **34**(4), 185–188.

Hsu, Y.-J. et al., 2006. Frictional afterslip following the 2005 Nias-Simeulue earthquake, Sumatra, *Science*, **312**(5782), 1921–1926.

Jónsdottir, K., Lindman, M., Roberts, R., Lund, B. & Bödvarsson, R., 2006. Modelling fundamental waiting time distributions for earthquake sequences, *Tectonophysics*, **424**(3–4), 195–208.

Jónsson, S., 2008. Importance of post-seismic viscous relaxation in southern Iceland, *Nat. Geosci.*, **1**(2), 136–139.

Jónsson, S., Segall, P., Pedersen, R. & Björnsson, G., 2003. Post-earthquake ground movements correlated to pore-pressure transients, *Nature*, **424**(6945), 179–183.

Kagan, Y.Y., 2004. Short-term properties of earthquake catalogs and models of earthquake source, *Bull. seism. Soc. Am.*, **94**(4), 1207–1228.

Kagan, Y.Y. & Houston, H., 2005. Relation between mainshock rupture process and Omori's law for aftershock moment release rate, *Geophys. J. Int.*, **163**(3), 1039–1048.

Kanamori, H. & Brodsky, E.E., 2004. The physics of earthquakes, *Rep. Prog. Phys.*, **67**(8), 1429–1496.

Kisslinger, C., 1996. Aftershocks and fault-zone properties, *Adv. Geophys.*, **38,** 1–36.

Lennartz, S., Bunde, A. & Turcotte, D.L., 2008. Missing data in aftershock sequences: explaining the deviations from scaling laws, *Phys. Rev. E,* **78**(4), 041115, doi:10.1103/PhysRevE.78.041115.

Li, V.C., Seale, S.H. & Cao, T., 1987. Postseismic stress and pore pressure readjustment and aftershock distributions, *Tectonophysics*, **144**(1–3), 37–54.

Lindman, M., Lund, B., Roberts, R. & Jónsdottir, K., 2006. Physics of the Omori law: inferences from interevent time distributions and pore pressure diffusion modeling, *Tectonophysics,* **424**(3–4), 209–222.

Lolli, B. & Gasperini, P., 2006. Comparing different models of aftershock decay: the role of catalog incompleteness in the first times after mainshock, *Tectonophysics,* **423**(1–4), 43–59.

Lund, B. & Slunga, R., 1999. Stress tensor inversion using detailed microearthquake information and stability constraints: application to Ölfus in southwest Iceland, *J. geophys. Res.*, **104**(B4), 14 947–14 964.

Nanjo, K.Z., Enescu, B., Shcherbakov, R., Turcotte, D.L., Iwata, T. & Ogata, Y., 2007. Decay of aftershock activity for Japanese earthquakes, *J. geophys. Res.,* **112**(B8), B08309, doi:10.1029/2006JB004754.

Narteau, C., Byrdina, S., Shebalin, P. & Schorlemmer, D., 2009. Common dependence on stress for the two fundamental laws of statistical seismology, *Nature*, **462**(7273), 642–645.

Neuzil, C.E., 2003. Hydromechanical coupling in geologic processes, *Hydrogeology Journal*, **11**(1), 41–83.

Nur, A. & Booker, J.R., 1972. Aftershocks caused by fluid flow? *Science*, **175**(4024), 885–887.

Ogata, Y., 1988. Statistical models for earthquake occurrences and residual analysis for point processes, *J. Am. Stat. Assoc.*, **83**(401), 9–27.

Okada, Y., 1992. Internal deformation due to shear and tensile faulting in a half-space, *Bull. seism. Soc. Am.*, **82**(2), 1018–1040.

Omori, F., 1894. On aftershocks of earthquakes, *J. Coll. Sci. Imp. Univ. Tokyo*, **7,** 111–200.

Pandee, A.P. & Chadha, R.K., 2003. Surface loading and triggered earthquakes in the Koyna-Warna region, western India, *Phys. Earth planet. Inter.*, **139**(3–4), 207–223.

Peng, Z., Vidale, J.E. & Houston, H., 2006. Anomalous early aftershock decay rate of the 2004 Mw6.0 Parkfield, California, earthquake, *Geophys. Res. Lett.,* **33**(17), L17307, doi:10.1029/2006GL026744.

Peng, Z., Vidale, J.E., Ishii, M. & Helmstetter, A., 2007. Seismicity rate immediately before and after main shock rupture from high-frequencey waveforms in Japan, *J. geophys. Res.*, **112**(B3), B03306, doi:10.1029/2006JB004386.

Perfettini, H. & Avouac, J.-P., 2004. Postseismic relaxation driven by brittle creep: a possible mechanism to reconcile geodetic measurements and the decay rate of aftershocks, application to the Chi-Chi earthquake, Taiwan, *J. geophys. Res.,* **109**(B2), B02304, doi:10.1029/2003JB002488.

Piombo, A., Martinelli, G. & Dragoni, M., 2005. Post-seismic fluid flow and Coulomb stress changes in a poroelastic medium, *Geophys. J. Int.*, **162**(2), 507–515.

Pollitz, F.F. & Sacks, I.S., 1996. Viscosity structure beneath northeast Iceland, *J. geophys. Res.*, **101**(B8), 17 771–17 793.

Rice, J.R. & Cleary, M.P., 1976. Some basic stress diffusion solutions for fluid-saturated elastic porous media with compressible constituents, *Rev. Geophys. Space Phys.*, **14**(2), 227–242.

Roeloffs, E.A., 1988. Fault stability changes induced beneath a reservoir with cyclic variations in water level, *J. geophys. Res.*, **93**(B3), 2107–2124.

Saar, M.O. & Manga, M., 2003. Seismicity induced by seasonal groundwater recharge at Mt. Hood, Oregon, *Earth planet. Sci. Lett.*, **214**(3–4), 605–618.

Scholz, C.H., 2002. *The Mechanics of Earthquakes and Faulting,* 2nd edn, Cambridge University Press, Cambridge.

Segall, P., 1985. Stress and subsidence resulting from subsurface fluid withdrawal in the epicentral region of the 1983 Coalinga earthquake, *J. geophys. Res.*, **90**(B8), 6801–6816.

Segall, P., 1989. Eartquakes triggered by fluid extraction, *Geology*, **17**(10), 942–946.

Shapiro, S.A., Patzig, R., Rothert, E. & Rindschwenter, J., 2003. Triggering of seismicity by pore-pressure perturbations: permeability-related signatures of the phenomenon, *Pure appl. Geophys.,* **160**(5–6), 1051–1066.

Shaw, B.E., 1993. Generalized Omori law for aftershocks and foreshocks from a simple dynamics, *Geophys. Res. Lett.*, **20**(10), 907–910.

Shcherbakov, R., Turcotte, D.L. & Rundle, J.B., 2004. A generalized Omori's law for earthquake aftershock decay, *Geophys. Res. Lett.*, **31**(11), L11613, doi:10.1029/2004GL019808.

Sigmundsson, F., 1991. Postglacial rebound and asthenosphere viscosity in Iceland, *Geophys. Res. Lett.*, **18**(6), 1131–1134.

Sigmundsson, F. & Einarsson, P., 1992. Glacio-isostatic crustal movements caused by historical volume change of the Vatnajokull ice cap, Iceland, *Geophys. Res. Lett.*, **19**(21), 2123–2126.

Talwani, P. & Acree, S., 1985. Pore pressure diffusion and the mechanism of reservoir-induced seismicity, *Pure appl. Geophys.*, **122**(6), 947–965.

Utsu, T., 1961. A Statistical Study on the Occurrence of Aftershocks, *Geophys. Mag.*, **30,** 521–605.

Utsu, T., Ogata, Y. & Matsuura, R.S., 1995. The centenary of the Omori formula for a decay law of aftershock activity, *J. Phys. Earth*, **43**(1), 1–33.

Vogfjord, K., 2003. Triggered seismicity after the June 17, Mw=6.5 earthquake in the South Iceland Seismic Zone: the first 5 minutes, *Geophys. Res. Abstr.,* **5,** 11251.

Wang, H.F., 2000. *Theory of Linear Poroelasticity,* Princeton University Press, Princeton.

Woessner, J. & Wiemer, S., 2005. Assessing the quality of earthquake catalogues: estimating the magnitude of completeness and its uncertainty, *Bull. seism. Soc. Am.*, **95**(2), 684–698.

Woessner, J., Hauksson, E., Wiemer, S. & Neukomm, S., 2004. The 1997 Kagoshima (Japan) earthquake doublet: a quantitative analysis of aftershock rate changes, *Geophys. Res. Lett.,* **31**(3), L03605, doi:10.1029/2003GL018858.

Yamashita, T. & Knopoff, L., 1987. Models of aftershock occurrence, *Geophys. J. R. astr. Soc.*, **91**(1), 13–26.

Zoback, M.D. & Harjes, H.P., 1997. Injection-induced earthquakes and crustal stress at 9 km depth at the KTB deep drilling site, Germany, *J. geophys. Res.*, **102**(B8), 18477–18491.

Zoback, M.D. & Healy, J.H., 1984. Friction, faulting and "in situ" stress, *Ann. Geophys.*, **2**(6), 689–698.